X-ray diffraction study of lattice strain in Fe/Au(001) superlattice films

1993 J. Phys.: Condens. Matter 5 1173

(http://iopscience.iop.org/0953-8984/5/9/002)

J. Phys.: Condens. Matter 5 (1993) 1173–1186. Printed in the UK

X-ray diffraction study of lattice strain in Fe/Au(001) superlattice films

N Nakayama†, T Okuyama‡ and T Shinjo
Institute for Chemical Research, Kyoto University, Uji 611, Japan

Received 28 August 1992, in final form 30 November 1992

Abstract. X-ray diffraction analyses of Fe/Au(001) superlattice films have revealed a body-centred tetragonal (BCT) structure with $c/a = 1.1$ for Fe layers thinner than 1.0 nm when Au layer thicknesses are 3.0 nm. The perfect in-plane lattice matching was confirmed by off-axial measurements. The observed in-plane lattice parameter, $a = 0.2875$ nm for BCT Fe, is close to the lattice dimension of bulk BCC Fe. However, profile analyses of axial scans have indicated that the Fe(002) lattice spacing along the growth direction has expanded. Such a tetragonal distortion cannot be explained by the normal elastic theory. The observed BCT structure of Fe would be a transient state on the BCC–FCC deformation path stabilized by a size effect or an interface effect. The tetragonal distortion is almost relaxed when Fe layers are thicker than 2.0 nm.

1. Introduction

Metallic superlattice films show many novel properties such as perpendicular magnetic anisotropy, giant magnetoresistance, or super-modulus effect [1, 2]. For the structural characterization of superlattice films, x-ray diffraction is one of the most convenient non-destructive methods for getting information on an atomic scale [3, 4]. Particularly, analysis of the lattice strain is very important in discovering the origin of perpendicular magnetic anisotropy or the super-modulus effect. In the usual x-ray diffraction studies, diffraction profiles are observed with the scattering vector perpendicular to the film plane and are analysed to get strain information along the growth direction. For strain analysis, it is important to know the precise in-plane lattice periodicity from x-ray diffraction measurements. Only a few measurements of in-plane lattice periodicity have been reported [5–9]. In this paper, we present the results of x-ray diffraction measurements of lattice strain both in the plane and along the growth direction for Fe/Au(001) superlattice films grown on GaAs(001) substrates [10].

2. Structural aspect of Fe/Au(001) superlattices

The epitaxial growth of the Fe/Au system has long been investigated [11]. Ultra-thin Fe films grow on Au(001) substrate in a layer by layer mode with the following epitaxial orientation relationship

FCC Au(001) // BCC Fe(001) FCC Au[110] // BCC Fe[100]. (A)

† Present address: Department of Chemistry, Faculty of Science, Kyoto University, Kyoto 606, Japan.
‡ Present address: TOYOBO Research Institute, TOYOBO Corp., 2-1-1 Katata, Ohtsu 520-02, Japan.

0953-8984/93/091173+14$07.50

The lattice mismatch, $[d(200)_{Fe} - d(220)_{Au}]/d(220)_{Au}$, is very small, being −0.6%. Dislocation-free growth has been reported for 1.0–2.0 nm thick Fe films [11]. Other BCC 3d-metal/FCC noble-metal thin-film systems, such as Fe/Ag [12, 13], and Cr/Au [14, 15], show the same epitaxial orientation relationship. Fabrications of superlattice films for these systems have been reported by several researchers [12, 14, 16]. In superlattice films, the orientation relationship (A) is retained.

Because of small in-plane lattice misfits of these BCC–FCC epitaxial systems, large lattice strains in superlattice films are not plausible. However, noteworthy lattice strains for Cr/Au and Ag/Fe systems have been reported. For the Cr/Au system, an x-ray diffraction analysis for superlattice films has revealed a lattice expansion of more than 7% in very thin Cr layers along the growth direction [14]. Also for the Fe/Ag system, a lattice expansion of 6% in 4ML Fe films on Ag(100) has been found by an XPS (x-ray photoelectron spectroscopy) forward scattering measurement [13].

In the present study, we have observed large lattice expansion (nearly 10%) along the growth direction for very thin Fe layers in Au/Fe superlattice films. The in-plane lattice periodicity was also measured by x-ray diffraction in the off-axial geometry. However, they indicated perfect coherence and rather small strain in the film plane.

3. Experimental details

Samples were prepared by electron beam evaporation in an ultrahigh vacuum of about 10^{-7} Pa. Films were grown on GaAs(001) wafer treated by the normal polishing procedure. Before deposition of the multilayer, a buffer layer of 100 nm thick Au single-crystal film was deposited at 200 °C. After the substrate was cooled down to room temperature, multilayers were deposited. The details of sample preparation including RHEED (reflection high-energy electron diffraction) characterizations have been reported elsewhere [10]. In the present investigation, we have used five samples with nominally designed structures of Au(10 nm)/[Fe(x nm)/Au(2.9 nm)]$_n$/Au(100 nm)/GaAs(001). The designed thicknesses of Au layers in the periodic multilayers are always 2.9 nm. The designed Fe layer thicknesses (x) were 3.0, 2.0, 1.4, 0.9 and 0.6 nm, respectively. The number of repetitions (n) is 10, 10, 40, 20 and 20, respectively.

X-ray diffraction experiments were performed by a conventional powder diffractometer (Rigaku RAD-II) and a four-circle diffractometer (Huber 420/511). The powder diffractometer was equipped with a diffracted beam monochromator of graphite 00.2 crystal. It was used for the axial scan measurements with the scattering vector perpendicular to the film plane (ordinary θ–2θ scans). The four-circle diffractometer was used for off-axial measurements. Copper Kα radiation (λ = 1.541 84 Å) from a rotating-anode type generator (Rigaku RU300) was used for both measurements.

In the off-axial measurements, the incident beam from the line source was monochromatized by a flat graphite 00.2 crystal and was collimated by two rectangular slits with a horizontal dimension of 0.5 mm and a vertical dimension of 4 mm. The diffracted beam intensities were measured by a scintillation counter. Two rectangular slits measuring 0.5 × 10 mm were placed between the sample and detector. The samples were mounted so that the (110)* reciprocal lattice plane of the FCC Au buffer layer coincides with the equatorial plane of the four circles. After the fine adjustment of the sample orientation with χ and ϕ axes, the angles of these two

axes were fixed. The angles of the detector (2θ) and specimen (ω) were computer controlled to scan along the arbitrary line on the (110)* reciprocal lattice plane. The schematic diagram of the Au(110)* reciprocal lattice plane is shown in figure 1(*a*). The growth direction $[001]^*_{Au}$ is denoted by the Q_y axis and the in-plane $[110]^*_{Au}$ direction is denoted by the Q_x axis. The units of both the Q_x and Q_y axes are momentum transfer $Q = 4\pi \sin \theta/\lambda$, measured in nm^{-1}. The relationships between 2θ, ω, Q_x and Q_y are

$$Q^2 = Q_x^2 + Q_y^2 \qquad 2\theta = 2 \sin^{-1}(Q\lambda/4\pi) \qquad \omega = \tan^{-1}(Q_x/Q_y) + \theta.$$

The schematic scattering geometry for the Au113 reflection is shown in figure 1(*b*). The scans were performed along lines parallel to the Q_y axis. The measurements are restricted within the reflecting geometry because of strong x-ray absorption by the GaAs substrate. The arch line in figure 1(*a*) shows the boundary between the reflecting and transmitting geometry. The Au113 reflection has the largest d-value among those that can be observed in the asymmetrically reflecting geometry. Actual scans were performed in the regions (A) and (B) shown in figure 1(*a*).

4. Results and discussion

4.1. X-ray diffraction profiles of an [Au(2.9 nm)/Fe(0.9 nm)]$_{20}$ superlattice film

The samples used in the present investigation have single-crystalline structures. The diffraction profiles for a sample with a nominal structure of [Au(2.9 nm)/Fe(0.9 nm)]$_{20}$ in figures 1(*c*) and 1(*d*) clearly indicate its single-crystalline structure. These figures show two-dimensional distributions of diffracted intensities around Au002 and Au113 reflections on the (110)* reciprocal lattice plane of FCC Au. Each intensity contour map was obtained from 14 line scans parallel to the Q_y axis.

Diffraction peaks from the superlattice are as sharp as the Au002 peak from the buffer layer as shown in figure 1(*c*). The fundamental reflection at $(Q_x, Q_y) = (0.00, 33.30)$ has a full width at half maximum (FWHM) of $\Delta Q_y = 0.26\ nm^{-1}$ and $\Delta Q_x = 0.60\ nm^{-1}$. The value of ΔQ_y indicates that the crystallographic coherence length along the growth direction is longer than 30 nm. The origins of peak broadening along the Q_x axis are the limited in-plane coherence length and the orientation distribution (mosaicity) of crystallites [17]. The observed peak widths along the Q_x axis are nearly the same as or smaller than that of the Au002 reflection. Therefore, the crystallinity of the superlattice is almost determined by the crystallinity of the Au buffer layer. The satellite peaks are all located on the Q_y axis and therefore there is no terracing effect as reported for some GaAs/AlAs semiconductor superlattices [18]. The superlattice period Λ determined from the average satellite spacing $\delta Q_y = 1.71\ nm^{-1}$ is 3.67 nm. It is to be noted that the satellite spacing is not commensurate with the fundamental reflection at $Q_y^0 = 33.3\ nm^{-1}$; namely $Q_y^0/\delta Q_y = 18.4$. The incommensurability suggests a fluctuation in the layer thicknesses [19, 20].

Satellite peaks are also observed around the Au113 reflection as shown in figure 1(*d*). The fundamental reflection is located at $(Q_x, Q_y) = (21.85, 49.90)$. The Q_y-value for the fundamental $(113)_0$ reflection satisfies a commensurate relation with that of the $(002)_0$ fundamental reflection; namely $Q_y(113) = 1.5\ Q_y(002)$. The average satellite spacing $\delta Q_y = 1.71\ nm^{-1}$ is the same as that of the $(002)_n$

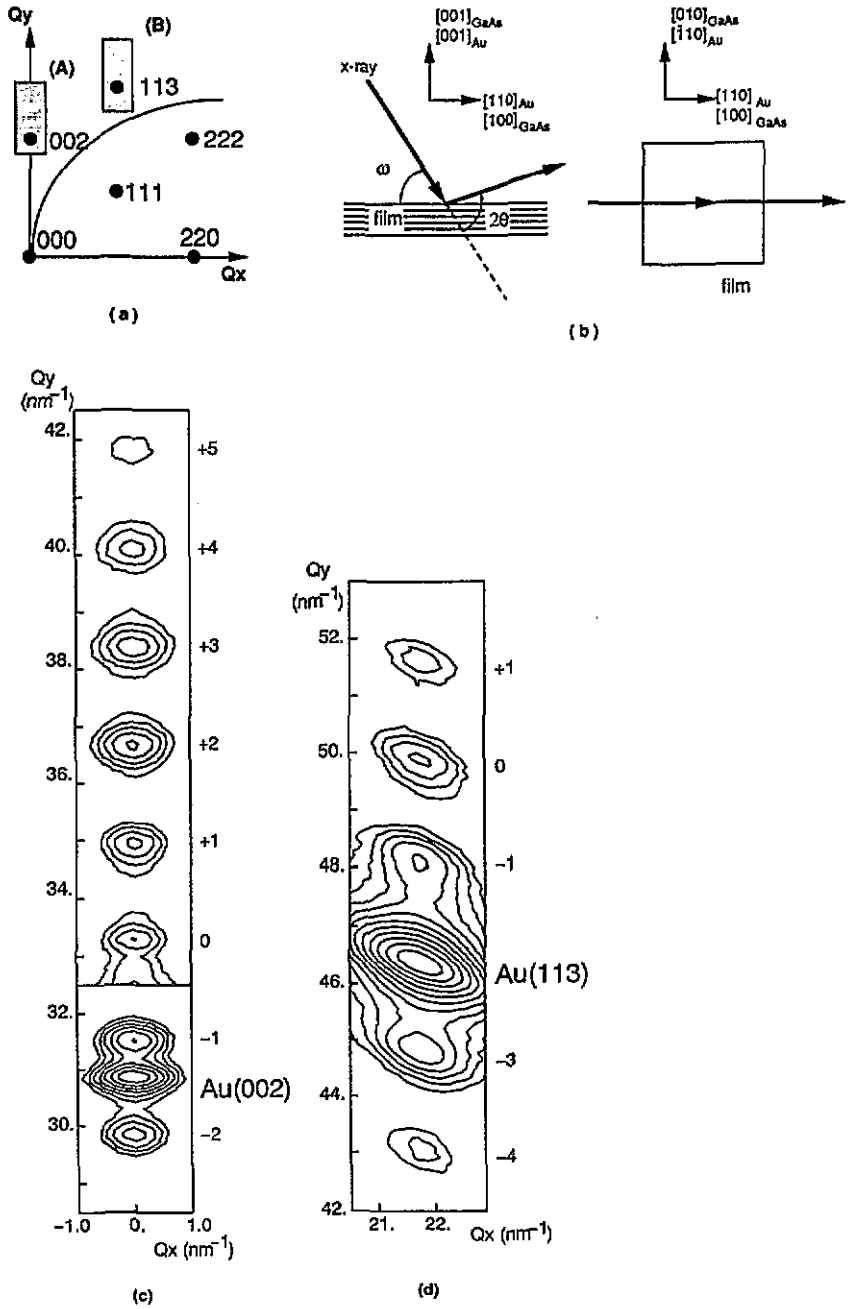

Figure 1. Off-axial x-ray diffraction measurements on the $(110)^*_{Au}$ reciprocal lattice plane for an [Au(2.9 nm)/Fe(0.9 nm)]$_{20}$/Au(100 nm) superlattice film. The Q_y axis and Q_x axis denote respectively the Au[001]* and Au[110]* directions with momentum transfer measured on a nm^{-1} scale. (*a*) The schematic $(110)^*_{Au}$ reciprocal lattice plane. Several line scans in the regions A and B were performed to obtain intensity contours in (*c*) and (*d*). The arch line shows the boundary between reflecting and transmitting geometries, $Q_y^2 = 4\pi Q_x/\lambda - Q_x^2$, for measurements using Cu Kα radiation. (*b*) The schematic diagrams of off-axial diffraction geometry. (*c*) The observed intensity distribution of $(002)_n$ superlattice reflections and Au002 reflection from the buffer layer. (*d*) The observed intensity distribution of $(113)_n$ superlattice reflections and Au113 reflection from the buffer layer. The contour steps in (*c*) and (*d*) are on a logarithmic scale. The number attached to each peak in (*c*) and (*d*) is the order of satellite reflection (n).

reflections. Because of a small distribution in the orientation of crystallites, the observed intensity distribution shows a broadening along a circle with its centre at the origin of the reciprocal lattice [17]. All the observed reflections are on a line $Q_x = 21.85 \pm 0.05$ nm^{-1}, which means that both in-plane Au(110) and Fe(100) lattice spacings are 0.2875 ± 0.0007 nm. The observed in-plane lattice spacing of the superlattice is in between the (110) lattice spacing of bulk FCC Au (0.2883 nm) and the (100) lattice spacing of bulk BCC Fe (0.2867 nm). The present Au/Fe superlattice is single-crystalline and shows perfect lattice matching in the film plane.

4.2. Satellite peak intensities of an [Au(2.9 nm)/Fe(0.9 nm)]$_{20}$ superlattice film

To investigate atomic structures in the superlattice, we have compared the satellite intensities with calculated ones. The diffraction profiles were calculated using a model structure shown in figure 2, which was based on a simple step model [3, 4]. However, we could not obtain good agreement when the lattice spacings along the growth direction were the same as those in the bulk metals.

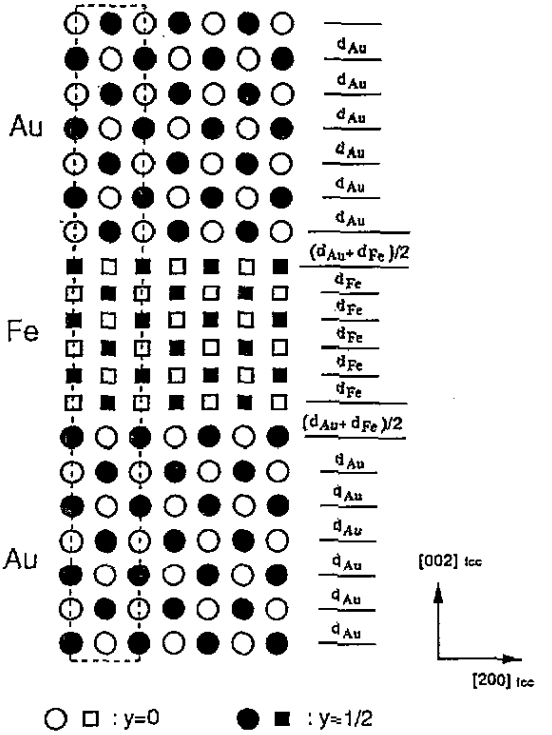

Figure 2. A step model for the atomic structure of an [Au(2.9 nm)/Fe(0.9 nm)] superlattice viewed along the [010] direction of FCC Au. The unit cell is marked with dotted lines. Circles and squares show Au and Fe atoms, respectively. The open symbols show atoms at $y = 0$ and full ones at $y = 0.5$. For values of other crystallographic parameters, see the text.

Figure 3 shows the observed axial scan profile (Q_y-scan with $Q_x = 0.0$) and two calculated diffraction profiles. The diffraction profiles were calculated using the

following formulae

$$I(Q) = |F(Q)|^2 L(Q) Lp \tag{1}$$

$$F(Q) = f_{Au}(Q)\sigma_{Au}\frac{\sin(Qn_{Au}d_{Au}/2)}{\sin(Qd_{Au}/2)}\exp(iQn_{Au}d_{Au}/2) + f_{Fe}(Q)\sigma_{Fe}\frac{\sin(Qn_{Fe}d_{Fe}/2)}{\sin(Qd_{Fe}/2)}\exp(iQn_{Fe}d_{Fe}/2) \tag{2}$$

$$L(Q) = \sin^2(NQ\Lambda/2)/\sin^2(Q\Lambda/2) \tag{3}$$

$$Lp = (1 + \cos^2 2\theta_m \cos^2 2\theta)/\sin 2\theta \tag{4}$$

where d_{Au}, d_{Fe} are lattice spacings, σ_{Au}, σ_{Fe} are atomic densities in the lattice plane, n_{Au}, n_{Fe} are numbers of lattice planes in a unit period, f_{Au}, f_{Fe} are atomic scattering factors and 2θ, $2\theta_m$ are the angles of the detector and monochromator.

In the calculations, the numbers of lattice planes in a unit period were fixed to be $n_{Au} = 14$ and $n_{Fe} = 6$, which gives layer thicknesses close to the designed ones. The atomic densities were also fixed to be $\sigma_{Au} = \sigma_{Fe} = 12.02$ atom nm^{-2}, which was calculated from the observed in-plane lattice spacing of 0.2875 nm. The lattice spacing at the interface was $(d_{Fe} + d_{Au})/2$. The value of d_{Au} was fixed to be 0.2039 nm (the lattice spacing in bulk Au metal) because a subsequent qualitative examination indicates large lattice strain only in the Fe layers. The diffraction intensity formula for superlattices, equation (2), indicates that the superlattice reflections have fairly strong intensities near $Q_y = 2\pi/d_{Au}$ and $Q_y = 2\pi/d_{Fe}$. The 002 diffraction peaks of bulk Au and Fe metals are located at $Q_y = 30.7$ nm^{-1} and 43.7 nm^{-1}, respectively, as marked in figure 3. The observed profile in figure 3(*a*) shows two intense peaks around $Q_y = 31$ nm^{-1} close to the bulk Au002 peak. However, the satellite peaks in the Q_y range greater than 40 nm^{-1} are very weak although measurements were limited up to 42.5 nm^{-1} because of the very strong GaAs 004 peak at $Q_y = 43.8$ nm^{-1}. Conversely, satellite peaks at around $Q_y = 36$ nm^{-1} show fairly large intensities, indicating the large lattice strain in Fe layers.

Figures 3(*b*) and 3(*c*) show two typical calculated profiles. Dotted lines show the structure factors $|F(Q)|^2$. The calculated profile (*b*) for strained Fe layers (d_{Fe} = 0.158 nm) well reproduces the observed profile. In particular, the satellite peaks at around $Q = 36$ nm^{-1} show fairly large intensities when $d_{Fe} = 0.1580$ nm. The intense peaks are located at around $Q = 40$ nm^{-1} when the Fe layers are not strained (d_{Fe} = 0.1433 nm), as was expected from the above mentioned qualitative argument. The above results suggest a nearly 10% expansion of Fe lattice spacing along the growth direction.

Peak intensities of the off-axial scan profile also suggest the large lattice strain in the Fe layer. Figure 4 shows the observed Q_y-scan profile with $Q_x = 21.85$ nm^{-1} and two calculated profiles. The lattice spacings of Fe are 0.158 and 0.1433 nm for the calculated profiles (*b*) and (*c*), respectively. The unit cell shown in figure 2 was assumed. The values of d_{Au}, σ_{Au}, σ_{Fe}, n_{Au} and n_{Fe} are the same ones as for the calculated profiles in figure 3. The profile (*b*) for $d_{Fe} = 0.1580$ nm shows intense higher-order satellites at around $Q_y = 58$ nm^{-1} and the profile (*c*) for $d_{Fe} = 0.1433$ nm does not show intense satellites in the Q_y-range. The observed higher-order satellites were too weak to be compared with calculated ones. However, observed intensity ratios around the Au113 reflection are close to those in profile (*b*).

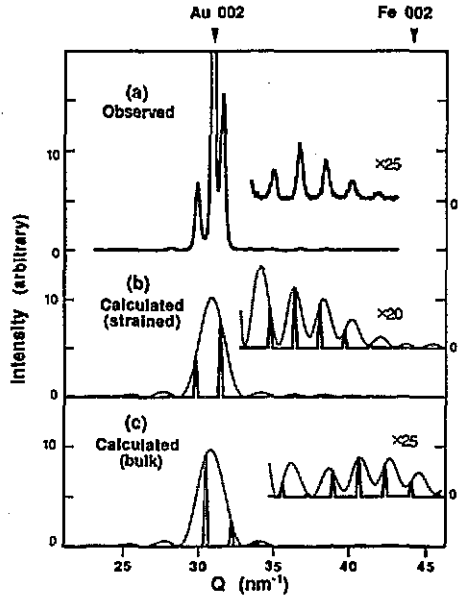

Figure 3. Axial scan profiles for an [Au(2.9 nm)/Fe(0.9 nm)] superlattice (Q_y scan profiles at $Q_x = 0$): (*a*) the observed profile; (*b*) a calculated profile for $d_{Fe} = 0.158$ nm (strained); (*c*) a calculated profile for $d_{Fe} = 0.143$ nm (bulk BCC Fe). Dotted lines show the structure factor $|F(Q)|^2$. The two line diagrams in each figure are the same ones to show the weak higher-order satellites on a linear scale on the right-hand axis.

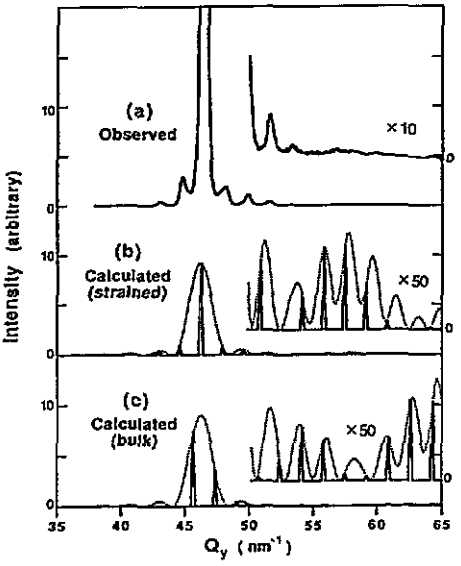

Figure 4. Off-axial scan profiles for an [Au(2.9 nm)/Fe(0.9 nm)] superlattice (Q_y scan profiles at $Q_x = 21.85$ nm^{-1}): (*a*) the observed profile; (*b*) a calculated profile for $d_{Fe} = 0.158$ nm (strained); (*c*) a calculated profile for $d_{Fe} = 0.143$ nm (bulk BCC Fe). Dotted lines show the structure factor $|F(Q)|^2$. The two line diagrams in each figure are the same ones to show the weak higher-order satellites on a linear scale on the right-hand axis.

4.3. Least-square fitting procedure of observed profiles

To obtain much more quantitative values of lattice spacing along the growth direction in both Au and Fe layers and also to investigate the effect of layer thickness on lattice strain, the observed axial scan profiles of five samples with different Fe layer thicknesses have been analysed by a profile fitting method. The simple step model (equations (1)–(4)) giving the commensurate satellite spacings cannot be used for the profile fitting procedure because of the incommensurability of the observed satellite spacings. The principal source of the incommensurability is a discrete fluctuation of layer thickness as discussed in much of the literature [3, 4, 17, 19, 20, 21, 22]. It seems

that the effect of continuous fluctuations is small for single-crystalline superlattices like the present samples.

For the calculation of theoretical profiles including the effect of discrete fluctuation, the Hendricks–Teller formula [3, 17, 23, 24] without neighbouring correlation was used. According to the formulas of Kakinoki and Komura [24], the theoretical diffraction intensity $I(Q)$ is given by

$$I(Q) = N D(Q) + H(Q) \tag{5}$$

where

$$D(Q) = \overline{V^2} + \overline{V^*}\,\overline{V\varphi}/(1-G) + \overline{V}\,\overline{V^*\varphi^*}/(1-G^*) \tag{6}$$

$$H(Q) = \overline{V^*}\,\overline{V\varphi}(G^N - 1)/(1-G)^2 + \overline{V}\,\overline{V^*\varphi^*}(G^{*N} - 1)/(1-G^*)^2 \tag{7}$$

$$\overline{V^2} = \sum_s \omega(s)|F_s(Q)|^3 \tag{8}$$

$$\overline{V} = \sum_s \omega(s) F_s(Q) \tag{9}$$

$$\overline{V\varphi} = \sum_s \omega(s) F_s(Q) \exp(-\mathrm{i}Q\Lambda_s) \tag{10}$$

and

$$G = \sum_s \omega(s) \exp(-\mathrm{i}Q\Lambda_s). \tag{11}$$

The thickness, structure factor, and the probability of the sth kind of unit layer are denoted by Λ_s, $F_s(Q)$ and $\omega(s)$, respectively. The step model was assumed for the structure of each unit layer, with the structure factor $F_s(Q)$ for each being given by equation (2). The asterisks in equations (6) and (7) denote complex conjugates. The first term in equation (5) (equation (6)) gives the main contribution to the diffracted intensity including the first-order diffuse scattering term and is identical to the original equation derived by Hendricks and Teller [23]. The second term (equation (7)) gives the higher-order term of diffuse scattering.

The number of lattice planes, n_{Fe} and n_{Au}, in the sth kind of unit layer and its probability, $\omega(s) = \omega_s(n_{\mathrm{Fe}}, n_{\mathrm{Au}})$, were calculated from the average layer thickness D_{Fe} and D_{Au} and its mean square deviation ΔD_{Fe} and ΔD_{Au} assuming the following Gaussian distribution functions.

$$G(n_{\mathrm{Fe}}) = \left(1/\sqrt{2\pi\Delta D_{\mathrm{Fe}}}\right) \exp\left\{-(n_{\mathrm{Fe}} d_{\mathrm{Fe}} - D_{\mathrm{Fe}})^2/2\Delta D_{\mathrm{Fe}}^2\right\}$$

$$G(n_{\mathrm{Au}}) = \left(1/\sqrt{2\pi\Delta D_{\mathrm{Au}}}\right) \exp\left\{-(n_{\mathrm{Au}} d_{\mathrm{Au}} - D_{\mathrm{Au}})^2/2\Delta D_{\mathrm{Au}}^2\right\}$$

$$\omega_s(n_{\mathrm{Fe}}, n_{\mathrm{Au}}) = G(n_{\mathrm{Fe}})G(n_{\mathrm{Au}}) / \sum_s G(n_{\mathrm{Fe}})G(n_{\mathrm{Au}}).$$

The layer units in which $G(n_{\mathrm{Fe}})$ and/or $G(n_{\mathrm{Au}})$ are less than 0.02 were discarded. For simplicity, the thickness dependences of lattice spacings were ignored and therefore d_{Fe} and d_{Au} are the average Fe and Au lattice spacings. The N in equation (5) is

a non-integral number of coherent unit layers. The average period $\bar{\Lambda}$ and the actual average layer thicknesses $\overline{D}_{Fe}$ and $\overline{D}_{Au}$ are given by

$$\bar{\Lambda} = \sum_s \omega_s(n_{Fe}, n_{Au})(n_{Fe}d_{Fe} + n_{Au}d_{Au})$$

and

$$\overline{D}_{Fe} = \sum_s \omega_s(n_{Fe}, n_{Au})n_{Fe}d_{Fe}$$

$$\overline{D}_{Au} = \sum_s \omega_s(n_{Fe}, n_{Au})n_{Au}d_{Au}.$$

The contribution of the Au buffer layer (given by equation (12) below) was also taken into consideration. The profile function in the form of the modified Lorentzian (given by equation (13) below) was convoluted with $I(Q) + bI_{buf}(Q)$. In the numerical calculation of convolution, an FFT (fast Fourier transform) routine was used. The base line was approximated by a linear function $cQ + d$.

$$I_{buf}(Q) = f_{Au}^2(Q)\sigma_{Au}^{B2}\sin^2\left(n_{Au}^B Q d_{Au}^B/2\right)\Big/\sin^2\left(Q d_{Au}^B/2\right) \tag{12}$$

$$P(Q) = \left[1\Big/\left(1 + Q^2/\Delta Q_0^2\right)\right]^{\alpha} \tag{13}$$

$$I_{calc}(Q) = a\{[I(Q) + bI_{buf}(Q)]LpA(Q)\} \otimes P(Q) + cQ + d \tag{14}$$

$$A(Q) = 1 - exp(-2\mu t/\sin\theta) \tag{15}$$

where $\otimes$ in equation (14) denotes convolution. The absorption factor given by equation (15) is also incorporated. A revised Marquardt method was used for the non-linear least-square fitting calculations. The initial refinements were performed to minimize $\sum_i\{\log[I_{obs}(Q_i)] - \log[I_{calc}(Q_i)]\}^2$, because the structural parameters for Fe layers greatly affect the intensity of weak satellites in the Q_y-range greater than 35 nm^{-1}. The final refinements were performed to minimize $\sum_i\{[I_{obs}(Q_i) - I_{calc}(Q_i)]^2/I_{obs}(Q_i)\}$. The maximum number of fitting parameters is 18; ten structural parameters of superlattice (N, D_{Fe}, D_{Au}, ΔD_{Fe}, ΔD_{Au}, d_{Au}, d_{Fe}, σ_{Au}, and σ_{Fe}), three structural parameters of the buffer layer (n_{Au}^B, d_{Au}^B and σ_{Au}^B), two profile parameters (ΔQ_0 and α), and four scaling parameters (a, b, c and d).

The several parameters were fixed at the final stage of refinement for all the samples. The plane densities σ_{Au} and σ_{Fe} were fixed to be the observed value (12.0 atom nm^{-2}) for [Au(2.9 nm)/Fe(0.9 nm)]$_{20}$ and their thickness dependences were ignored because the misfit is very small. In fact, an RHEED study [10] of Fe film grown on Au(001) film indicates no significant change of the in-plane structure up to a thickness of 5.0 nm, within experimental error. The three structural parameters for buffer layers, n_{Au}^B, d_{Au}^B and σ_{Au}^B, were also fixed to be 200, 0.2038 nm and 11.5 atom nm^{-2}, respectively. Also, the two profile parameters ΔQ_0 and α were fixed to be 0.171 nm^{-1} and 2.0, respectively.

The number of coherent layers N was also fixed to be the actual number of layer pairs for each sample according to the following assumption. The observed peak widths of the fundamental reflections are fairly sharp for all the samples and give

tentative coherence lengths greater than 30 nm if they are calculated by the Scherrer formula. They correspond to a value of N nearly equal to 10. Under the present Hendricks–Teller formula, variation of N greater than 5 does not greatly change the profile shape and intensity ratios in the observed narrow Q_y-range. Therefore we have assumed that all the layers are coherently diffracting except a sample with nominally 1.5 nm thick Fe and with 40 layer pairs. The value of N for this sample was fixed to be one half of the actual number of layer pairs. By fixing N, the effects of N were incorporated in the root mean square deviation of the layer thicknesses ΔD_{Fe} and ΔD_{Au}. The final refinements were performed for the remaining ten parameters, D_{Fe}, D_{Au}, ΔD_{Fe}, ΔD_{Au}, d_{Au}, d_{Fe}, a, b, c and d.

4.4. Thickness dependence of structural parameters

The results of least-square fitting are shown in figure 5 and the final parameters are listed in table 1. The standard deviations for the final parameters are also shown in table 1. To evaluate the goodness of fit numerically, two R-factors defined by the following equations were calculated.

$$R_{\log} = \sum_i |\log[I_{calc}(Q_i)] - \log[I_{obs}(Q_i)]| \Big/ \sum_i \log[I_{obs}(Q_i)]$$

$$R_{lin} = \sum_i |I_{calc}(Q_i) - I_{obs}(Q_i)| \Big/ \sum_i I_{obs}(Q_i).$$

At least one of these R-factors is less than 20% for all the samples. We could not decrease the R-values further using the present structural model. Other structural factors should be incorporated in the calculation to obtain much better fits; such as the continuous fluctuation, the deviation of lattice spacings at the interface from $(d_{Fe} + d_{Au})/2$, the thickness dependences of d_{Fe} and d_{Au}, or correlations between neighbouring layer units.

Table 1. Fitting parameters for calculated profiles shown in figure 5. For the meaning of the fitting parameters, see the text. The numbers in parentheses show standard deviations.

Sample	(*a*)	(*b*)	(*c*)	(*d*)	(*e*)
Nominal Thickness of Fe (nm)	0.6	0.9	1.5	2.0	3.0
Fitting Parameters					
$\bar{\Lambda}$ (nm)	3.71(4)	3.66(6)	3.91(12)	4.55(2)	5.49(2)
d_{Fe} (nm)	0.1615(3)	0.1565(1)	0.1494(17)	0.1425(13)	0.1442(7)
d_{Au} (nm)	0.2033(1)	0.2031(2)	0.2027(2)	0.2026(2)	0.2021(2)
N	20	20	20	10	10
$\bar{D}_{Au}$ (nm)	2.99(2)	2.75(2)	2.79(10)	2.95(1)	2.95(1)
$\bar{D}_{Fe}$ (nm)	0.72(2)	0.91(4)	1.12(2)	1.60(1)	2.54(1)
ΔD_{Au} (nm)	0.13(2)	0.17(7)	0.12(12)	0.10(3)	0.08(4)
ΔD_{Fe} (nm)	0.14(2)	0.11(4)	0.12(15)	0.06(2)	0.04(2)
R_{lin} (%)	8.8	29.3	25.8	11.3	13.9
$R_{\log}$ (%)	16.6	18.7	17.9	28.1	29.2

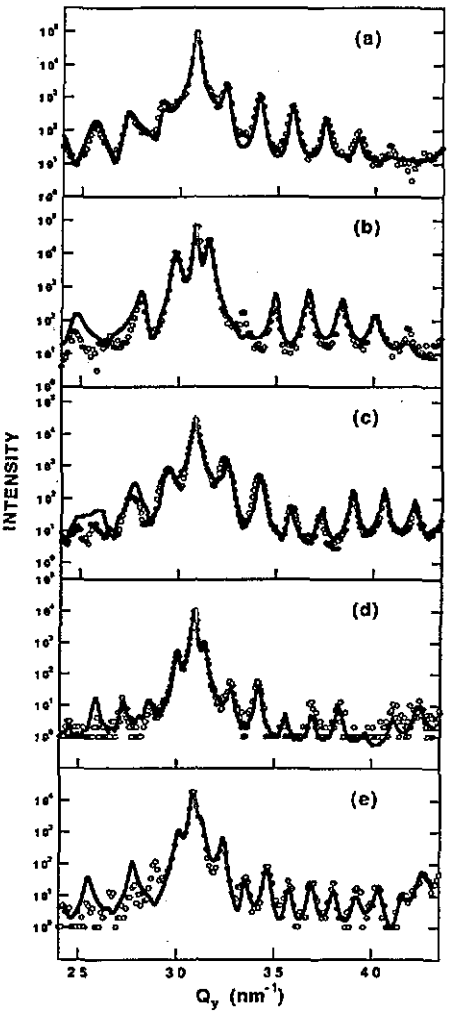

Figure 5. The thickness dependence of axial scan profiles for [Au(2.9 nm)/Fe(x nm)]$_n$/Au(100 nm) superlattice films. Nominal Fe layer thicknesses are (*a*) 0.6 nm, (*b*) 0.9 nm, (*c*) 1.5 nm, (*d*) 2.0 nm, and (*e*) 3.0 nm, respectively. Ordinates show logarithmic intensities. The line plots show the results of the least-square fitting calculations described in the text. The final parameters for the calculated profiles are listed in table 1.

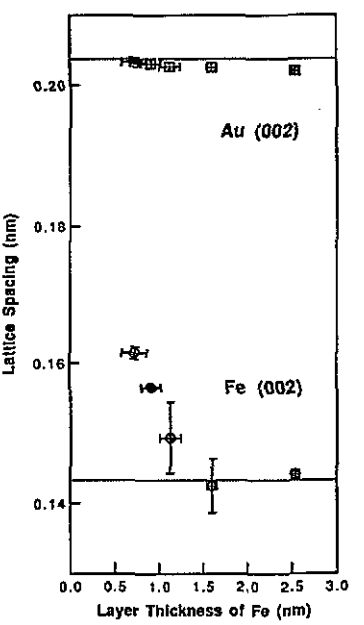

Figure 6. The thickness dependence of average Au and Fe lattice spacings d_{Au} and d_{Fe} in [Au(2.9 nm)/Fe(x nm)]$_{20}$/Au(100 nm) superlattice films. The error bars for the ordinate are the estimated standard deviations for d_{Fe} and d_{Au}. The abscissa shows $\overline{D}_{Fe}$ and its error bar shows ΔD_{Fe}.

However, judging from the estimated standard deviations shown in table 1, the present structural refinements give reliable values for the average lattice spacings d_{Fe} and d_{Au}. Figure 6 shows the thickness dependences of lattice spacings, d_{Au} and d_{Fe}. The abscissa shows the refined values of Fe layer thicknesses ($\overline{D}_{Fe}$). When nominal thickness is greater than 1.5 nm, the lattice spacing of Fe is close to the value of bulk BCC Fe. With decrease of nominal thickness the lattice spacing of Fe increases up to nearly 0.16 nm. The very thin Fe layers in Au/Fe(001) superlattices are strained.

The lattice strain in the Fe layers will be discussed in the next section. The refined value of d_{Au} decreases with increasing Fe layer thickness. However at the present stage it may be concluded that the lattice spacings of the nearly 3 nm thick Au layers are independent of the Fe layer thickness and that they are slightly smaller than the value for the bulk metal.

The refined values of average periods $\Lambda = \overline{D}_{Au} + \overline{D}_{Fe}$ are always smaller than the designed periods, indicating some errors in the layer thickness calibration. A systematic deviation from designed values is recognized for Fe layers. When the designed Fe layers are thicker than 2.0 nm, the refined values are about 20% smaller than the designed value. With decrease of designed thickness, the difference between designed and refined values decreases. This fact correlates with the increase of lattice spacing d_{Fe} because the designed thickness was determined from weight measurements by a quartz oscillator thickness monitor.

The estimated layer-thickness fluctuations ΔD_{Fe} and ΔD_{Au} are not more than 0.2 nm. Such one- or two-monolayer deviations are plausible under the present sample preparation condition. The values of ΔD_{Fe} and ΔD_{Au} for samples (*a*), (*b*) and (*c*) are larger than those for samples (*d*) and (*e*). It seems that the uncertainty in layer thickness increases with the number of layer pairs. Particularly, sample (*c*) with 40 layer pairs shows irregular peak broadening for satellites located at Q_y smaller than 35 nm^{-1}. Although the effect of layer number on the layer thickness fluctuation seems important in investigating the growth mode in this system, it is beyond the scope of this paper.

4.5. Lattice strain of very thin Fe layer

The results of least-square fitting have revealed lattice expansion along the growth direction for Fe layers thinner than 1.5 nm. Namely, Fe layers thinner than 1.5 nm have body centred tetragonal (BCT) structures. For nominally 0.9 nm thick Fe layers, the in-plane lattice spacing estimated from off-axial measurement is 0.2875 nm and the average (001) lattice spacing along the growth direction is 0.313 nm. The axial ratio c/a for BCT Fe is nearly equal to 1.1.

Such a large lattice expansion along the growth direction cannot be ascribed to the in-plane coherency strain because the lattice misfit is very small (0.6%) for the orientation relationship (A). Furthermore, the larger Au lattice spacing causes tensile stress for the Fe layers. Therefore, elastic theory predicts not lattice expansion but lattice contraction along the growth direction.

The effect of intermixing at the interface seems to be negligible. The bulk-phase diagram of Au–Fe alloy shows very limited solubility of Au in BCC Fe and the reported lattice parameter of a quenched $Fe_{95}Au_5$ BCC solid solution is 0.2897 nm [25]. Also, the magnetization of the present superlattice films are not much different from that of bulk BCC Fe even when the Fe layers are 0.6 nm thick [10].

The formation of metastable face centred tetragonal (FCT) Fe is also not plausible. The observed c/a value, 1.1, for 0.9 nm thick BCT Fe layers corresponds to a c/a ratio of 0.78 for FCT Fe. The lattice strain is very large if FCC Fe is assumed. Recently, the structures of very thin epitaxial FCC Fe films deposited on Cu(001) substrates have been investigated extensively [26–28]. The reported lattice dimension of FCC Fe is about 0.36 nm and small tetragonal distortions due to the coherency strain were revealed by LEED (low-energy electron diffraction) experiments [27]. The lattice misfit of the FCC Fe/Cu(001) system is very small and is −0.6%. In the case

of pseudomorphic growth of (001)-oriented FCC Fe on Au(001), the misfit is about −13%. It is expected that such a large lattice misfit would cause a large lattice strain not only in the Fe layer but also in the Au layers, even when superlattices were deposited on a 100 nm thick Au buffer layer. Also it is to be noted that the FCT lattice is not a Bravais lattice and that it can be reduced to a BCT lattice which is one of the Bravais lattices.

Anyway, it may be concluded at the present stage that a transient BCT Fe structure on the so-called Bain deformation path from a BCC to an FCC lattice is stabilized by a size effect or interface effect in Au/Fe(001) superlattices. The observed relaxation of the BCT structure to the BCC structure along with an increase in Fe layer thickness strongly suggest an interface electronic-structure effect. Recently, many studies on the metastable BCT structure of very thin metal films have been reported in addition to the examples mentioned in section 2. The overgrowth of FCT(BCT) Cu films on Pt(001) and Pd(001) substrates with a large misfit of about 9% has been investigated by detailed LEED analyses [29, 30]. The axial ratio c/a for BCT Cu on Pt(001) is nearly 1.15. Also, the BCT structure of Cu in the Ag/Cu system has been studied by EXAFS measurements [31]. As for superlattice systems, the BCT structure of Mn in Ag/Mn(001) superlattices has been revealed by a detailed x-ray diffraction profile analysis [22, 32]. It has been reported that the BCT structure of Mn relaxes with increase of layer thickness similarly to the behaviour of the Au/Fe system [22].

5. Conclusion

We have observed an anomalous lattice strain of very thin Fe layers in Fe/Au(001) superlattice films as well as the reported one for very thin Cr layers in Cr/Au(001) superlattices. *The in-plane lattice spacing observed by off-axial x-ray diffraction* measurements indicates that there exists only a small in-plane coherency strain. The in-plane coherency strain is not the origin of large lattice strain along the growth direction. The observed anomalous lattice strain indicates that a BCT phase on the *Bain deformation path between FCC and BCC structures is stabilized by an interface* effect. The BCT structure relaxes to form a BCC structure with the increase of thickness up to 2.0 nm. Similar BCT–BCC transformations with increase of thickness are expected for very thin Cr layers in Cr/Au(001) superlattices and also for Fe layers in Fe/Ag(001) superlattices. More quantitative x-ray diffraction investigations of three-dimensional structures are desirable for these superlattice systems having ultra-thin layers with BCT structures. Also, the correlation of tetragonality with magnetic properties is an interesting theme for a future investigation.

Acknowledgment

This work was supported by a Grant in Aid for Scientific Research on Priority Area (Nos 0225413, 03240103, 04224103) from the Ministry of Education, Science and Culture of Japan.

References

[1] Shinjo T 1991 *Surf. Sci. Rep.* **12** 49–98
[2] Schuller I K 1988 *Physics, Fabrication and Application of Multilayered Structures* ed P Dhez and C Weisbuch (New York: Plenum) p 139
[3] McWhan D B 1988 *Physics, Fabrication and Application of Multilayered Structures* ed P Dhez and C Weisbuch (New York: Plenum) p 67
[4] Fujii Y 1987 *Metallic Superlattices: Artificially Structured Materials* ed T Shinjo and T Takada (Amsterdam: Elsevier) p 33
[5] Gyorgy E M, McWhan D B, Dillon J J F, Walker L R and Waszczak J V 1982 *Phys. Rev.* B **25** 6739
[6] Lee C H, He H, Lamelas F J, Vavra W, Uher C and Clarke R 1989 *Phys. Rev. Lett.* **62** 653
[7] Lamelas F J, Lee C H, He H, Vavra W and Clarke R 1989 *Phys. Rev.* B **40** 5837
[8] Bain J A, Chyung L J, Brennan S and Clemens B M 1991 *Phys. Rev.* B **44** 1184
[9] Engel B N, Wiedmann M H, Van Leeuwen R A, Falco C M, Wu L, Nakayama N and Shinjo T 1992 *Appl. Surf. Sci.* **60/61** 776
[10] Okuyama T 1991 *Japan. J. Appl. Phys.* **30** 2053
[11] Wassermann E F and Jablonski H P 1970 *Surf. Sci.* **22** 69
[12] Gutierrez C J, Wieczorek M D, Tang H, Qiu Z Q and Walker J C 1991 *J. Magn. Magn. Mater.* **99** 215
[13] Egelhoff J W F, Jacob I, Rudd J M, Cochran J R and Heinrich B 1990 *J. Vac. Sci. Technol.* A **8** 1582
[14] Bisanti P, Brodsky M B, Felcher G P, Grimsditch M and Sill L R 1987 *Phys. Rev.* B **35** 7813
[15] Durbin S M, Berman L E, Batterman B W, Brodsky M B and Hamaker H C 1988 *Phys. Rev.* B **37** 6672
[16] Kikuchi H, Suzuki Y and Katayama T 1990 *J. Appl. Phys.* **67** 5403
[17] Moritani I, Nakayama N and Shinjo T 1990 *J. Phys.: Condens. Matter* **2** 9717
[18] Neumann D A, Zabel H and Morkoç H 1988 *J. Appl. Phys.* **64** 3024
[19] Schuller I K, Grimsditch M, Chamber F, Devane G, Vanderstraeten H, Neerinck D, Locquet J-P and Bruynseraede Y 1990 *Phys. Rev. Lett.* **65** 1235
[20] Window B 1988 *J. Appl. Phys.* **63** 1080
[21] Locquet J-P, Neerinck D, Stockman L, Bruynseraede Y and Schuller I K 1989 *Phys. Rev.* B **39** 13 338
[22] Fullerton E E, Schuller I K, Vanderstraeten H and Bruynseraede Y 1992 *Phys. Rev.* B **45** 9292
[23] Hendricks S and Teller E 1942 *J. Chem. Phys.* **10** 147
[24] Kakinoki J and Komura Y 1952 *J. Phys. Soc. Japan* **7** 30
[25] Villars P and Calvert L D 1985 *Pearson's Handbook of Crystallographic Data for Intermetallic Phases* (Am. Soc. for Metals: Ohio)
[26] Lu S H, Quinn J, Tian D, Jona F and Marcus P M 1989 *Surf. Sci.* **209** 364
[27] Jona F and Marcus P M 1989 *Surf. Sci.* **223** L897
[28] Thomassen J, Feldmann B and Wuttig M 1992 *Surf. Sci.* **264** 406
[29] Li H, Wu S C, Tian D, Quinn J, Li Y S, Jona F and Marcus P M 1989 *Phys. Rev.* B **40** 5841
[30] Li Y S, Quinn J, Tian D and Jona F 1991 *Phys. Rev.* B **44** 8261
[31] Jiang D T, Crozier E D and Heinrich B 1991 *Phys. Rev.* B **44** 6401
[32] Jonker B T, Krebs J J and Prinz G A 1989 *Phys. Rev.* B **39** 1399